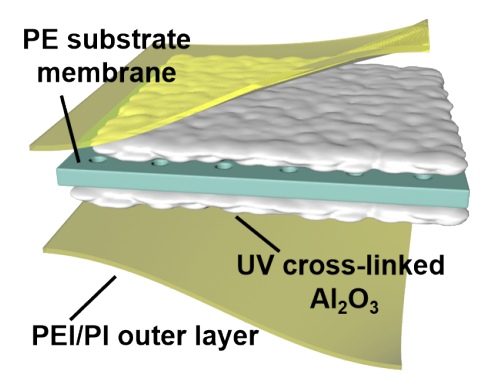


Research Article

Modulating interphasial chemistry through PEI/PI separator coating for thermally robust high-voltage batteries

Shuofeng Jian, Jiahui Zeng, Chen Guo [⊠], Zhaohuang Zhan, Yumeng Lan, Zu-Wei Yin, Hai Lin [⊠], Luyi Yang [⊠], and Feng Pan [⊠]

Graphical Abstract



A trilayer polyetherimide (PE)-Al $_2$ O $_3$ -polyetherimide/polyimide (PEI/PI) separator, namely PAP, is designed for high-voltage and high-temperature lithium-ion batteries. The outer PEI/PI coating layer regulates the interfacial solvation structure of Li $^+$ and facilitates desolvation, enabling the formation of a robust and thermally stable cathode–electrolyte interphase. The intermediate Al $_2$ O $_3$ ceramic layer enhances electrolyte affinity and structural integrity. This synergistic architecture endows the LiCoO $_2$ cathode with exceptional cycling stability at 4.6 V and 60°C.

Address correspondence to Chen Guo, guoc@senior798.com; Hai Lin, linhai@pkusz.edu.cn; Luyi Yang, yangly@pkusz.edu.cn; Feng Pan, panfeng@pkusz.edu.cn

Received: August 15, 2025 Revised: August 25, 2025 Accepted: September 5, 2025



Read Online



Citation: Jian S., Zeng J., Guo C., et al. Modulating interphasial chemistry through PEI/PI separator coating for thermally robust high-voltage batteries. *Energy Mater. Devices*, 2025, 3(4), 9370077. https://doi.org/10.26599/EMD.2025. 9370077

Research Article

https://doi.org/10.26599/EMD.2025.9370077

Modulating interphasial chemistry through PEI/PI separator coating for thermally robust high-voltage batteries

Shuofeng Jian¹, Jiahui Zeng¹, Chen Guo² [⋈], Zhaohuang Zhan¹, Yumeng Lan¹, Zu-Wei Yin³, Hai Lin¹ [⋈], Luyi Yang¹ [⋈], and Feng Pan¹ [⋈]

- ¹ School of Advanced Materials, Peking University Shenzhen Graduate School, Shenzhen 518055, China
- ² Shenzhen Senior Technology Material Co., LTD, Shenzhen 518106, China
- ³ College of Energy, Xiamen University, Xiamen 361005, China

Received: August 15, 2025 / Revised: August 25, 2025 / Accepted: September 5, 2025

ABSTRACT

Lithium-ion batteries are essential for modern energy storage, yet achieving simultaneous high-temperature and high-voltage operation remains challenging due to interfacial compatibility. In this study, we introduce a polyetherimide (PEI)–polyimide (PI) functional coating on the separator that enhances wettability, thermal stability, and mechanical strength, while markedly improving cathode stability under harsh conditions. By integrating theoretical calculations with experimental validation, we demonstrate that the PEI/PI coating modulates the solvation structure of lithium-ions, thereby facilitating the interfacial desolvation process. More importantly, the PEI/PI layer regulates electrolyte decomposition at the interface, promoting the formation of a uniform and thermally stable cathode–electrolyte interphase. Consequently, LiCoO₂ cathodes exhibit improved cycling performance at 60°C. Overall, this work underscores the pivotal role of separator coatings in governing interfacial chemistry and provides a viable strategy for designing high-performance lithium-ion batteries capable of enduring both high temperatures and high

KEYWORDS

high-voltage batteries, high-temperature performance, separators, interfacial solvation structure, cathode–electrolyte interphase

1 Introduction

With the widespread application of lithium-ion batteries (LIBs) in new energy vehicles and grid energy storage systems, challenges related to their safety under high-temperature and high-voltage operating conditions have become increasingly critical^[1-3]. Under rapid charging and discharging or during other demanding operating scenarios, the internal temperature of the battery can rise to levels exceeding 60°C^[4-6]. Such temperature elevation initiates severe oxidative decomposition of the electrolyte and intensifies parasitic reactions at the electrode–electrolyte interface. These include transitionmetal dissolution as well as rupture and reformation of the solid–electrolyte interphase (SEI) and the cath-

ode–electrolyte interphase (CEI), ultimately resulting in accelerated capacity fade and an increased likelihood thermal runaway^[7–9]. To address this issue, researchers have sought to enhance the interfacial stability of high-energy-density battery systems at elevated temperatures through electrolyte design (e.g., localized high-concentration electrolytes^[10] and electrolyte additives^[11]), as well as protective cathode interface coatings^[12].

The separator is not only a passive physical barrier that prevents internal short circuits by isolating the anode and cathode but also an active component that directly influences the lithium-ion transport and interfacial electrochemical reactions during battery operation^[7,13–15]. Given its close contact with both electrodes, the separator plays a crucial role in determin-

Address correspondence to Chen Guo, guoc@senior798.com; Hai Lin, linhai@pkusz.edu.cn; Luyi Yang, yangly@pkusz.edu.cn; Feng Pan, panfeng@pkusz.edu.cn

[©] The Author(s) 2025. Published by Tsinghua University Press. The articles published in this open access journal are distributed under the terms of the Creative Commons Attribution 4.0 International License (http://creativecommons.org/licenses/by/4.0/), which permits use, distribution and reproduction in any medium, provided the original work is properly cited.

ing the thermal and electrochemical stability of LIBs, particularly at elevated temperatures. For instance, poor electrolyte wettability and thermal shrinkage of conventional polyolefin-based separators can accelerate interfacial degradation and the formation of lithium dendrites^[16,17]. To overcome these issues, researchers have developed coated separators with improved thermal resistance and mechanical strength using ceramic or polymer layers^[16,18,19]. However, existing studies have concentrated on enhancing the thermal stability of separators, whereas their potential to regulate interfacial chemistry and electrochemical performance during high-temperature operation remains underexplored.

Moreover, various surface modification strategies have been developed for separator coatings, such as ceramic or polymer coatings, to enhance thermal stability. Although these approaches have been effective in improving performance, there are still significant limitations in terms of mechanical strength, interfacial adhesion, and scalability preparation[20,21]. For example, despite improving the heat resistance of the membrane, ceramic coatings often delaminate during long-term electrolyte immersion due to its weak interfacial bonding with the substrate. Polymer coatings, although flexible and chemically compatible, require complex and costly fabrication of ultrathin layers, which hinders the balance between performance and practicality^[22].

To overcome these limitations, we designed a gradient-functional sandwich separator in this work. This separator consists of a low-cost, high-porosity wet-processed polyethylene (PE) substrate, an Al₂O₃ interlayer that enhances interfacial bonding, and an ultra-thin polyetherimide/polyimide (PEI/PI) outer coating that serves as a high-temperature barrier for suppressing electrolyte side reactions[19,23]. Importantly, the outer coating is a blend of PEI and PI, which combines the strong film-forming ability and adhesion of PEI with the exceptional thermal and mechanical stability of PI, thereby improving the overall thermal stability of the separator^[24,25]. This synergistic multilayer architecture not only enhances thermal stability but also regulates the interfacial solvation structure through the PI coating layer, thereby forming more stabilized CEI and SEI layers and enabling the stable cycling in high-voltage lithium-metal batteries at elevated temperatures [7,26,27]. Accordingly, a trilayer polyetherimide (PE)-Al₂O₃polyetherimide/polyimide (PEI/PI) separator, namely PAP, is designed for high-voltage and hightemperature lithium-ion batteries. Our study highlights the separator's active role in modulating interfacial reactions, offering a novel strategy for enhancing the high-temperature durability and safety of LIBs.

2 Materials and methods

2.1 Experimental

The PE substrate was preheated at 60°C for 5 min, with its thickness monitored continuously using a thickness gauge (ScanTech Model X). A uniform Al₂O₃ particle dispersion was coated bilaterally via microgravure coating, followed by ultraviolet crosslinking (365 nm) for particle immobilization. Subsequently, a blend solution of PEI and PI (1:1 mass ratio, 8.3 wt% in N-methyl-2-pyrrolidone [NMP]) was prepared by magnetic stirring, and the molecular structure of PEI is shown in Fig. S1 in Material. Supplementary The Al₂O₃-coated membrane was dip-coated with the polymer solution and transferred to a coagulation bath (NMP/water = 40/60 in weight, 15°C) for 10 min to induce non-solvent-induced phase separation, thereby forming a porous polymer layer. Finally, the membrane was rinsed sequentially in ultrapure water baths (24°C) to remove residual NMP (<0.1 wt% by thermogravimetry analysis), yielding a PEI/PI multilayer composite membrane with controllable pore structure.

2.2 Materials characterizations

The morphology and elemental distribution of the samples were examined using a field-emission scanning electron microscope (SEM; Zeiss SUPRA-55). Cryogenic transmission electron microscopy (Cryo-TEM) images were obtained using a JEOL-3200FS microscope. The CEI of LiCoO₂ (LCO) particles after cycling was observed at -172°C with a cryo transfer tomography holder (Model 2550, Fischione). The chemical states of selected elements on the electrode surfaces were analyzed using X-ray photoelectron spectroscopy (XPS; Thermo Scientific Escalab 250Xi). During measurement, the analysis chamber was maintained at a base pressure below 3.0 × 10⁻¹⁰ mbar, and all binding energies were calibrated against the C 1s peak at 284.8 eV. Time-of-flight secondary ion mass spectrometry (TOF-SIMS) was conducted using a Nano TOF II instrument (ULVAC-PHI, Japan) with a Bi³⁺ primary ion beam (30 kV) for analysis and an Ar⁺ sputtering beam (3 keV, 100 nA) at a sputtering rate of 0.1 nm s⁻¹ to obtain depth profiles. Fourier-transform infrared (FTIR) spectroscopy was conducted using a Nicolet iS50 spectrophotometer, with the KBr pellet method. Raman spectra of the materials were collected using a miniature laser confocal Raman spectrometer (Horiba LabRAM HR800, France) with a 633 nm wavelength laser at room temperature. The powder X-ray diffraction (XRD) and in situ XRD measurements were conducted on a Bruker D8 Advance diffractometer with a Cu-Kα radiation source. Contact angle

measurements were conducted using an OCA 25 instrument (DataPhysics Instruments) to characterize the wettability of the separators and electrodes.

2.3 Electrochemical measurement

The cathode was prepared by blending LCO (80 wt%) with a conductive additive (acetylene black, 10 wt%) and polyvinylidene fluoride (PVDF; 10 wt%) binder in NMP to form a homogeneous slurry. This mixture was cast uniformly onto an aluminum foil current collector and dried under vacuum at 120°C for 12 h to ensure complete solvent removal. The mass loadings of active materials on the cathode were ≈2.2 mg cm⁻². Throughout this study, all coin cells were assembled in CR2032 configuration inside an argon-filled glovebox, employing lithium metal (anode), LCO (cathode), separator, and commercial electrolyte. The electrolyte was purchased from Guangzhou Tinci Materials Technology Co., Ltd (China). The assembled coin cells were subsequently assessed using a NEWARE battery test system under controlled temperatures of 25°C or 60°C. Electrochemical cycling of the LCO||Li cells was performed at 0.5 C (1 C = 210 mAh g^{-1}) for the initial five cycles. Electrochemical impedance spectroscopy (EIS) measurements were carried out on a Solartron Analytical 1470E workstation over a frequency range of 1000 kHz-0.1 Hz with an alternating current perturbation amplitude of 10 mV.

2.4 Computation details

To investigate the interfacial properties and adsorption behavior, first-principles calculations based on density functional theory (DFT) were performed using the Vienna Ab initio Simulation Package (VASP v6.4.2)[28-30]. The exchange-correlation interactions were described by the generalized gradient approximation in the Perdew-Burke-Ernzerhof formulation[31]. The interactions between ions and valence electrons were modeled with the projector augmented wave method[32], and the pseudopotentials were generated using VASPKIT[33]. A kinetic energy cutoff of 520 eV was applied to the planewave basis. The partial occupancies of the Kohn-Sham orbitals were determined using Gaussian smearing with a width of 0.02 eV. Spin polarization was applied to all calculations. All geometry optimizations were conducted at fixed lattice parameters with the conjugate-gradient algorithm, converging when forces dropped below 0.02 eV/Å. The electronic self-consistent field calculations converged at 10⁻⁵ eV. All calculations were conducted at 333 K. The Brillouin zone was sampled with a $1 \times 1 \times 1$ Monkhorst-Pack k-point mesh, appropriate for surface and low-dimensional models. To account for van der Waals interactions, the Grimme DFT-D3 dispersion correction scheme was employed[34]. All symmetry operations were turned off to prevent symmetry artifacts during adsorption modeling. The electrostatic potential distribution was extracted using the LOCPOT file. Structural and adsorption configurations were analyzed and visualized with VESTA^[35].

3 Results and discussion

3.1 Characterization of PEI/PI coated membrane

The schematic of the PAP membrane preparation process is presented in Fig. 1a. The PAP membrane preparation consists of sequential steps: unwinding PE substrate membrane, applying Al_2O_3 coating, ultraviolet cross-linking to immobilize particles, immersing the coated film in a coagulation bath, drying, and finally winding into the finished membrane. Critically, this fabrication strategy employs industry-compatible methods, namely, micro-gravure coating and non-solvent-induced phase separation, providing a practical pathway for large-scale production with minimal process. A full-scale roll of the PAP separator demonstrating industrial-scale production is displayed in Fig. S2 in Supplementary Material.

From the inside out, the as-prepared membrane consists of three main layers (Fig. 1b). The outer layer, composed of a PEI/PI blend, provides high mechanical strength and chemical stability, effectively resisting degradation under elevated temperatures and high-voltage operation. The interlayer comprises a 1.5 µm-thick Al₂O₃ coating cross-linked by ultraviolet irradiation, which improves electrolyte affinity and reinforces the structural integrity of the membrane. The inner layer is a 7 µm PE substrate with a microporous framework that facilitates efficient lithium-ion transport. The cross-sectional SEM image of the membrane (Fig. 1d) corroborates this trilayer PE-Al₂O₃-PEI/PI structure. To investigate the chemical composition of the PAP membrane, ex situ FTIR spectroscopy was conducted (Fig. 1c and Table S1 in Supplementary Material). In the 1730 cm⁻¹ region, the PAP membrane exhibited a distinct C=O stretching vibration peak, confirming the presence of imide groups and suggesting enhanced polarity^[22]. In addition, the C-N stretching vibration peak at 1200-1350 cm⁻¹ further verified the presence of amide linkages. A C=C stretching vibration peak (~1600 cm⁻¹) was also, indicating aromatic moieties in the polymer backbone. For comparison, the Celgard 2500 membrane (denoted as CG) was used as a control, and its cross-sectional SEM image is provided in Fig. S3 in Supplementary Material. As a corroborative experiment, XPS (Fig. S4 in Supplementary Material) confirmed the presence of imide

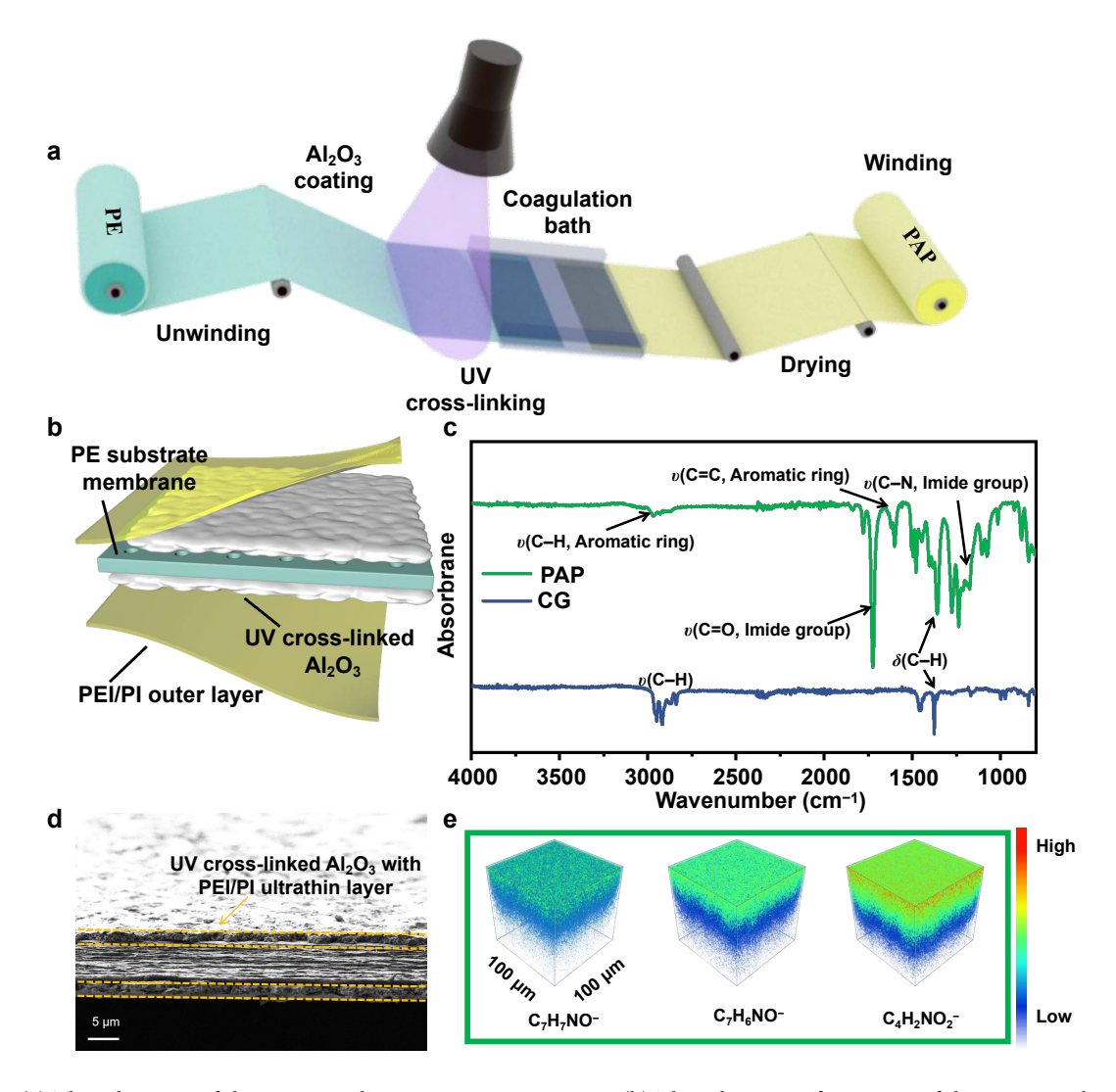


Figure 1 (a) The schematic of the PAP membrane preparation process. (b) The schematic of structure of the PAP membrane. (c) Ex situ FTIR spectra of the PAP membrane and CG membrane. (d) Cross-sectional SEM images of the PAP membrane. (e) The TOF-SIMS three-dimensional distributions of the pristine PAP membrane for $C_7H_7NO^-$, $C_7H_6NO^-$, and $C_4H_2NO_2^-$ fragments.

bonds (N–C=O) via a characteristic N 1s peak at 400.0 eV^[36]. In the C 1s spectra, binding energies at ~286.2 eV (C–C/C–H and C–O/C–N) and 288.4 eV (N–C=O) further confirmed imide formation on the membrane surface. The O 1s spectra displayed peaks at 532.0 eV (C=O) and 533.3 eV (C–O), consistent with the presence of both imide and ether bonds. Additionally, a distinct Al 2p peak at 74.5 eV verified the successful incorporation of Al $_2$ O $_3$ particles.

In addition to chemical composition of the coating layer, the spatial distribution of its components strongly influences the properties of the separator. TOF-SIMS (Fig. 1e) was employed to probe the spatial distribution of the coating components in the PAP membrane. High-molecular-weight fragments (e.g., C₇H₇NO⁻) were primarily localized near the membrane surface^[37]. As the molecular weight of the detected fragments decreased, their penetration depth progressively increased, indicating the presence of a molecular-weight gradient within the coat-

ing. Specifically, the surface layer was enriched in higher molecular weight PEI/PI species, while lower molecular weight components were more prevalent in the interior. This distribution further confirms that the improved electrolyte wettability and enhanced ion diffusion in the PAP membrane originate from the surface-localized PEI/PI coating.

In order to systematically assess the structural features and electrochemical performance of the composite membrane, we first measured its wettability with a carbonate-based electrolyte (56.34 wt% ethyl methyl carbonate [EMC], 29.74 wt% fluoroethylene carbonate [FEC], 0.42 wt% diethyl carbonate, and 13.5 wt% LiPF₆) and compared it with that of the commercial CG membrane (Fig. 2a). The CG membrane exhibits a contact angle of 68.7°, whereas the PAP membrane displayed a markedly lower value of 16.8°, demonstrating its superior electrolyte wettability. Moreover, the electrolyte droplets spread more rapidly and uniformly on the PAP

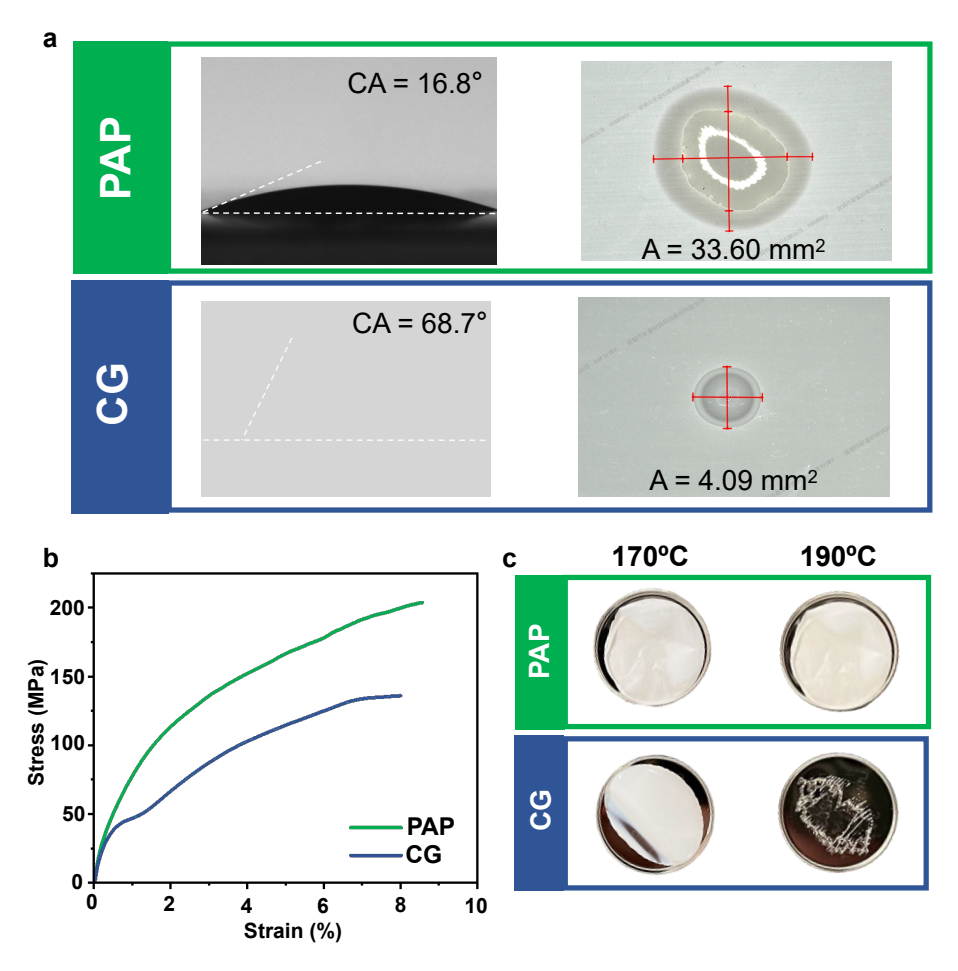


Figure 2 Physical characterization of the membranes. (a) Contact angles of electrolyte (left) and electrolyte spreading tests (right) on the surface of the PAP membrane and CG membrane. CA, contact angle; A, the spreading area of electrolyte droplets. (b) Stress–strain curves of the PAP membrane and the CG membrane. (c) Thermal shrinkage test of the PAP membrane and CG membrane.

membrane, producing a diffusion area of 33.6 mm², compared to only 4.09 mm² for the CG membrane. The significant difference indicates that the PAP membrane possesses a much stronger affinity toward the electrolyte. Next, FTIR spectroscopy was conducted to study the interaction between the separator and the electrolyte (Fig. S5 in Supplementary Material). For the membranes soaked in electrolyte, a blue shift of the PAP membrane absorption peaks was observed in the 830–850 cm⁻¹ region, suggesting that the characteristic peaks of the P–F vibration were altered by stronger coordination between the PAP membrane and the electrolyte components^[18].

The stress-strain curves (Fig. 2b) of the PAP membrane and the CG membrane confirm that the PAP membrane exhibited a markedly higher tensile strength, reaching a maximum stress of ~203 MPa. This result indicates that the multilayer composite architecture of the PAP membrane enhances both its tensile strength and deformation resistance, thereby enabling the membrane to maintain structural integrity during extended battery cycling. The results of the thermal shrinkage tests (Fig. 2c) demonstrated pronounced morphological differences between the

PAP and CG membranes when subjected to elevated temperatures of 170°C and 190°C^[20,21]. At 170°C, the PAP membrane exhibited a slight shrinkage, while the CG membrane underwent substantial shrinkage accompanied by partial melting of the polymer matrix. By 190°C, the morphology of the PAP membrane was almost identical to that at 170°C, further confirming its superior thermal stability. In contrast, the CG membrane was fully melted at 190°C, with no discernible morphology remaining, thereby highlighting its markedly inferior thermal stability compared to the PAP membrane.

The lithium-ion transference number ($t_{\rm Li+}$) serves as a key metric for assessing Li⁺ migration efficiency in electrolytes, directly influencing charge–discharge kinetics and long-term cycling stability^[38]. The test results in Fig. S6 in Supplementary Material indicated that the $t_{\rm Li+}$ of the PAP separator reached 0.540, exceeding that of the CG separator (0.343). This indicates that the PAP separator facilitates more efficient Li⁺ transport across the electrolyte–separator interface. Its gradient-functionalized structure (such as the polar groups in the PEI/PI outer layer) modulates the interfacial solvation environment, thereby

lowering the resistance to Li⁺ migration and ensuring stable cycling performance of high-voltage lithium metal batteries under elevated-temperature conditions.

3.2 Regulation of interfacial reactions

To further elucidate the mechanisms governing interfacial regulation in the PAP membrane, firstprinciples calculations based on DFT performed[30]. The influence of the PAP and CG on Li⁺ migration was analyzed in terms of four parameters: electrostatic potential distribution, adsorption behavior, desolvation energy, and diffusion dynamics. The PEI and polypropylene (PP) were considered as the representative surface components of the PAP membrane and the CG membrane, respectively. The electrostatic potential distribution (Fig. 3a) revealed distinct negative-potential regions at the C=O functional groups of PEI. These regions, elevated electrostatic potential values, exerted strong attraction toward positively charged species (e.g., Li⁺), thereby promoting Li⁺ enrichment at the membrane surface and enabling the formation of initial migration pathways. Conversely, PP exhibited a relatively uniform electrostatic potential distribution, lacking such localized negative potential clusters capable of anchoring Li+, thereby exhibiting limited Li⁺ adsorption capacity. Furthermore, as shown in Fig. S7 in Supplementary Material, the adsorption energy of Li⁺ on PEI was –2.19 eV, significantly lower than that on PP (–0.04 eV). This enhanced binding arises primarily from the abundant polar carbonyl (C=O) functional groups on the PEI chain, which act as electron-accepting sites, thereby stabilizing Li⁺ adsorption at the interface. In contrast, the molecular chain of PP was non-polar and lacked functional groups and thus failed to provide stable adsorption sites, resulting in weaker Li⁺ affinity.

The interfacial migration of Li involves a desolvation process. To further evaluate how PEI and PP regulate solvation-structure dissociation during Li+ migration, we calculated the desolvation energies of Li⁺-4EMC and Li⁺-4FEC complexes on their surfaces (Fig. 3b and Fig. S8 in Supplementary Material). The desolvation energies of Li+-4EMC and Li+-4FEC on the PEI surface were -0.71 and -0.83 eV, respectively, demonstrating a strong thermodynamic driving force for spontaneous desolvation. In contrast, the PP surface exhibited substantially higher desolvation energies, with values of +0.24 eV for Li⁺-4EMC and +1.55 eV for Li⁺-4FEC. This finding further validates that PEI synergistically promotes interfacial Li⁺ desolvation complementing its strong adsorption affinity and enhanced diffusion capacity. Next, we calculated the diffusion coefficients of Li+ on both

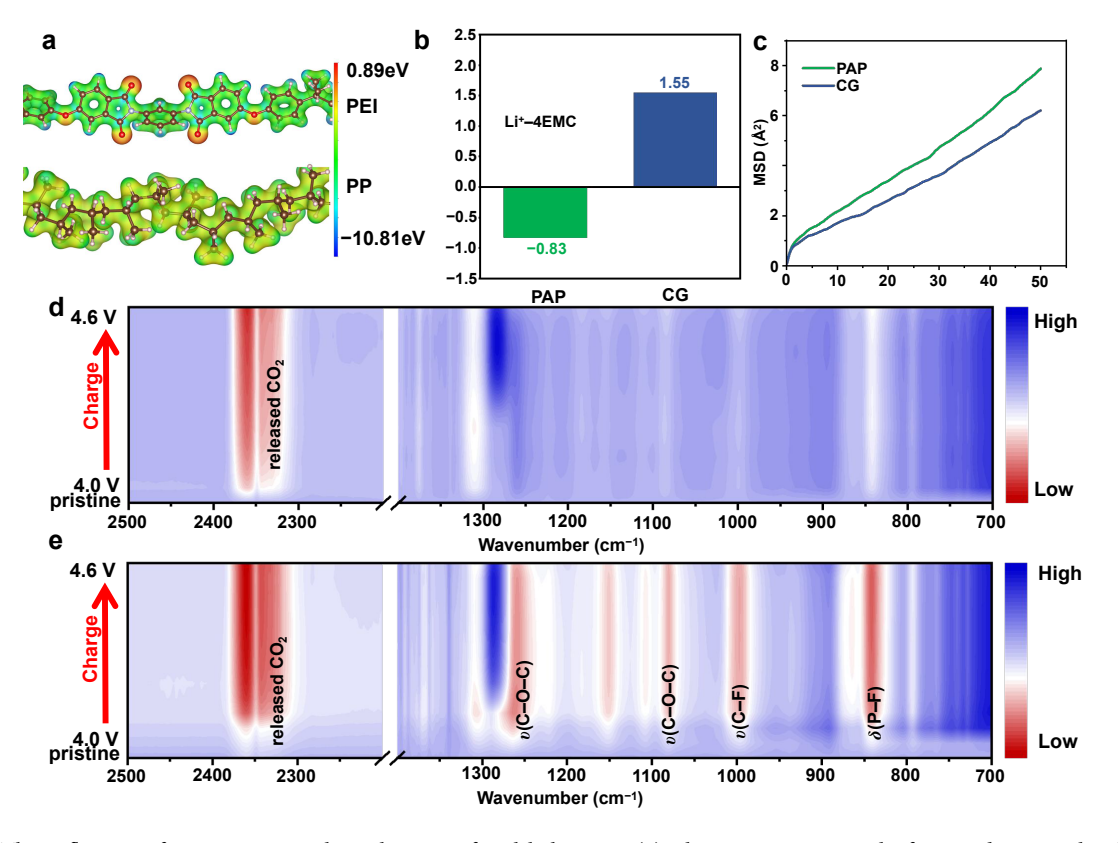


Figure 3 The influence of separators on electrolyte interfacial behaviors. (a) Electrostatic potential of PP and PEI molecular chain. (b) Calculated desolvation energy of Li⁺ for EMC in the PAP and CG. (c) Diffusion coefficient of Li⁺ for the PAP and CG. Comparison of *in situ* FTIR spectra with LCO under 4.6 V by the PAP separator (d) and the CG separator (e).

surfaces based on the adsorption-induced ionic distribution (Fig. 3c). The diffusion coefficient on the PAP membrane surface was 2.35×10^{-6} cm² s⁻¹, markedly exceeding that of the CG membrane surface (1.91×10^{-6} cm² s⁻¹). These findings reveal that the strong coordinative adsorption of Li⁺ on the PEI facilitates partial desolvation, effectively removing solvent molecules (e.g., EMC/FEC). This reduction in solvation-sheath size decreases the apparent ionic radius and diffusion barrier, thereby enabling higher interfacial migration flux and more efficient Li⁺ transport^[14].

In situ FTIR was employed to monitor separatorinduced solvation behavior during LCO||Li battery cycling, offering direct insights into electrolyte stability and interfacial reactions. As shown in Figs. 3d and 3e, in the 840–850 cm⁻¹ region, the PAP separator facilitated rapid conversion of POF₃ (P-F bending vibration peak) to inorganic CEI^[9], consistent with its lower desolvation energy^[23]. In contrast, the CG separator showed delayed POF₃ conversion owing to its higher desolvation energy. This resulted in persistent decomposition of interfacial organic species, as evidenced by pronounced attenuation of characteristic peaks in the 1000–1300 cm⁻¹ region, including the C-F vibrational peak at 1000 cm⁻¹, the C-O-C vibrational peak at 1100 cm⁻¹, and the C-O-C vibrational peak at 1260-1300 cm^{-1[12,39]}. The PAP separator, however, maintained stable peak intensities, confirming its ability to suppress solvent decomposition and preserve interfacial stability by accelerating favorable electrochemical processes. Additionally, at ~2350 cm⁻¹ (the peak of released CO₂), the PAP separator displayed a narrower and less intense signal than the CG separator, indicating mitigated CO₂ generation from solvent decomposition.

In situ EIS (Fig. S9 in Supplementary Material) demonstrated that the PAP separator facilitated rapid interfacial passivation in the initial cycle. The charge transfer impedance ($R_{\rm ct}$) of the PAP separator showed minimal variation, while $R_{\rm SEI/CEI}$ remained stable, confirming a better interfacial stability. In contrast, the CG separator exhibited pronounced impedance fluctuations during the charging process. In particular, at 4.6 V, the $R_{\rm ct}$ of the CG separator increased significantly, and the $R_{\rm SEI/CEI}$ continued to rise during discharge, indicating instability of the CEI layer and progressive degradation of battery performance.

3.3 Electrochemical performance at elevated temperature

At an elevated temperature of 60°C, a clear divergence in cycling stability emerged between PAP and CG (Fig. 4a). The cell with the PAP separator retained 168 mAh g⁻¹ after 200 cycles (68.9% capacity retention) with a high average Coulombic effi-

ciency of 99.4%. By contrast, declined significantly within several tens of cycles, accompanied by a gradual loss in Coulombic efficiency. The cycling performance of LCO||Li half-cells constructed with different separators was initially assessed at 25°C (Fig.4b). The cells assembled with the PAP and CG separators showed comparable initial specific capacities (~200 mAh g⁻¹) and nearly identical cycling stability for 250 cycles. The voltage profiles of LCO||Li halfcells assembled with the PAP (Fig. 4c) and CG (Fig. 4d) under 60°C highlighted the separator-dependent differences in interfacial stability and Li+ transport kinetics. For the cell with the PAP separator, the charge-discharge voltage plateaus remained stable, reflecting effective interfacial modulation and the formation of a robust CEI capable of withstanding high voltage and temperature. In contrast, the cell with the CG separator showed pronounced voltage polarization after 50 cycles, particularly in the 4.4-4.6 V region, indicating aggravated interfacial side reactions from CEI instability that elevated chargetransfer impedance and hindered Li⁺ transport. To directly visualize the mechanical stability of the separator coatings under extreme cycling conditions, SEM characterization was conducted after 100 cycles at 60°C and 4.6 V (Fig. S10 in Supplementary Material). The CG separator displayed severe cracking and structural damage, confirming mechanical degradation. In contrast, the PAP separator retained excellent structural integrity, with no visible cracks or delamination in the PEI/PI coating, demonstrating superior mechanical and electrochemical stability consistent with the sustained cycling performance in

To exclude the influence of the Li anode on cycling stability, Li||Li symmetric cells with both separators were assembled and assessed (Fig. S11 in Supplementary Material). Experimental results showed that at 25°C, both separators maintained comparable cycling stability for over 800 h. However, the PAP displayed a lower overpotential due to its superior Li⁺ conductivity. The impact of separators on rate capability was further evaluated at various C-rates (Fig. S12 in Supplementary Material). At low rate (0.2 C), both cells delivered nearly identical specific capacities. However, as the rate increases beyond 1 C, the PAP membrane demonstrated higher capacity. At 5 C, the cell assembled with PAP retained 150 mAh g⁻¹, whereas the CG-based cell delivered only 124 mAh g⁻¹. The excellent rate performance of the PAP is attributed to its enhanced lithium-ion transport capability.

Ex situ Raman spectroscopy was used to analyze the structural evolution of LCO cathodes after long-term cycling. For LCO cycled with the PAP separator (Fig. 4e), the Raman spectra showed well-preserved characteristic peaks associated with the

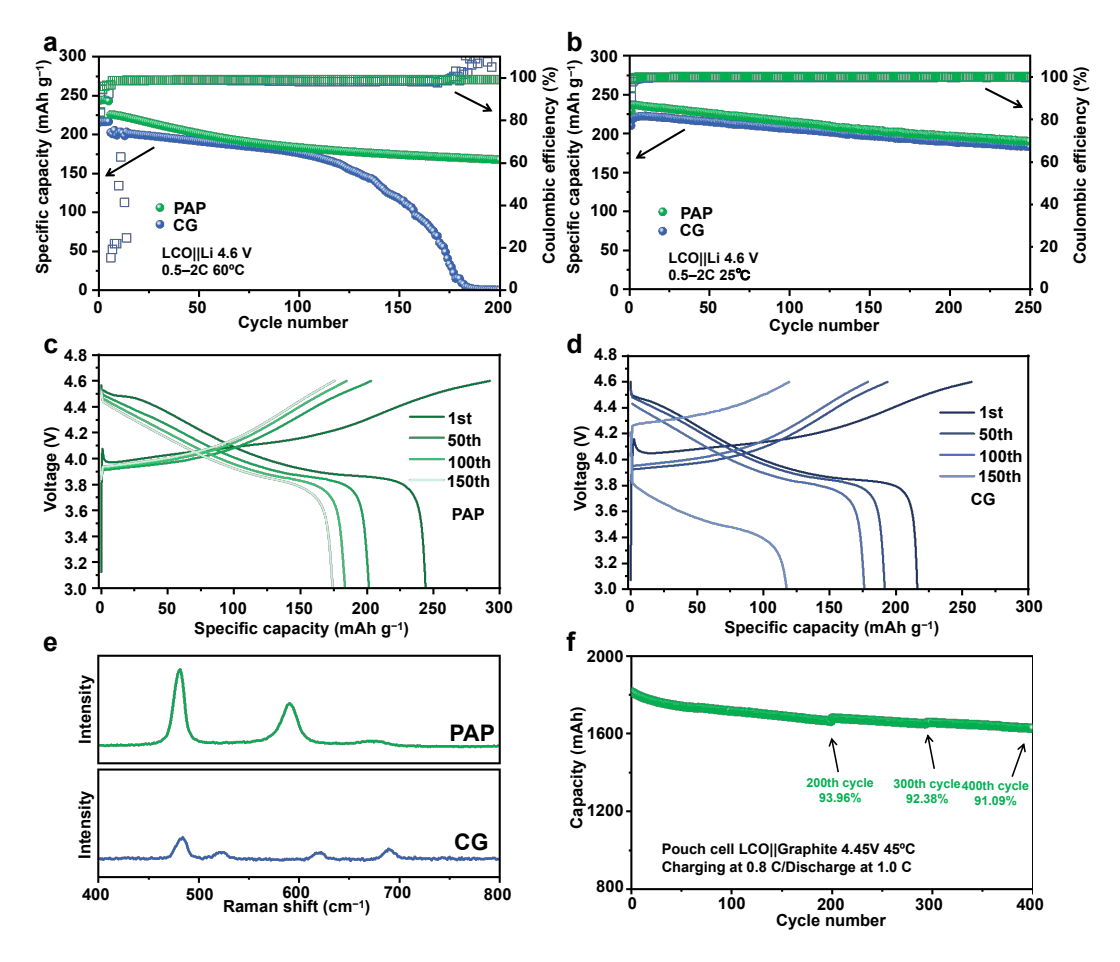


Figure 4 Electrochemical performances of LCO||Li batteries with different separators. Galvanostatic cycling performance and Coulombic efficiency of LCO||Li half-cells assembled with the PAP separator and the CG separator under 60°C (a) and 25°C (b). Voltage profiles of LCO||Li half-cells assembled with the PAP separator (c) and the CG separator (d) under 60°C. (e) *Ex situ* Raman spectra of cycled LCO by the PAP separator and the CG separator. Long-term cycling performance of the LCO||Graphite pouch cell employing the PAP separator under 4.45 V, 45°C (0.8 C charge/1.0 C discharge).

layered LCO structure. The intense peaks at ~480 and ~590 cm⁻¹, corresponding to the E_g (Co-O inplane stretching) and A_{1g} (Co-O out-of-plane stretching) modes of the hexagonal α-NaFeO₂ structure, retained high intensity with minimal shifts relative to pristine LCO^[40]. In contrast, the Raman spectra of LCO cycled with the CG (Fig. 4f) displayed marked peak broadening and reduced intensity at ~480 and ~590 cm⁻¹, along with the emergence of a broad ~650 cm⁻¹ peak characteristic of the spinel phase (Fd-3m symmetry)[41]. This confirmed a substantial layered-to-spinel phase transition in LCO, driven by uncontrolled interfacial reactions. The spinel phase possesses lower Li⁺ diffusion kinetics and reduced capacity, accounting for the rapid capacity decay observed in Fig. 4b.

To probe bulk structural evolution, *ex situ* XRD was performed for long-term cycled LCO electrodes (Fig. S13 in Supplementary Material). With the CG separator, the (003) peak of LCO shifted markedly to lower angles, indicating expansion of the c-lattice parameter due to irreversible structural transitions^[42,43]. In contrast, the LCO electrode paired

with the PAP separator exhibited a much smaller peak shift, confirming that the robust, inorganic-rich CEI promoted by PAP effectively suppresses parasitic reactions, limits lattice distortion, and improves LCO structural stability during high-voltage cycling.

A comparison with recent literature on advanced separators (summarized in Table S2 in Supplementary Material) underscores the outstanding performance of the PAP separator. Unlike most modified separators that maintain stability mainly under low-voltage operation and room temperature conditions^[14,44,45], the PAP separator achieves superior long-term cycling stability of high-voltage LCO at 60°C, even without electrolyte optimization.

To further validate the practical viability of the PAP separator, an LCO||Graphite pouch cell (~1.8 Ah) was fabricated and cycled at 4.45 V and 45°C. As illustrated in Fig. 4f, the cell equipped with the PAP separator delivered an initial discharge capacity of 1813 mAh and retained 91.3% (1628 mAh) after 400 cycles, corresponding to a capacity fade rate of 0.022% per cycle. The stable cycling performance confirms that the PAP separa-

tor stabilizes the CEI even in commercial-scale pouch cells, underscoring its strong potential for nextgeneration high-energy batteries designed to operate reliably under harsh conditions.

3.4 Characterizations of CEI

To elucidate the influence of the CEI on the interfacial stability of LCO, XPS analysis was conducted to examine its chemical composition. As shown in the C 1s spectra (Figs. 5a and 5d), the PAP separator, compared with the CG, yields reduced intensities of C=O (~288.4 eV), O-C=O (~289.0 eV), and C-O peaks (~286.2 eV) reflecting suppressed solvent decomposition. These organic byproducts, unlike inorganic species, readily dissolve into the electrolyte at elevated temperatures, triggering ongoing side reactions. Therefore, the CEI induced by the PAP separator exhibits superior thermal stability. Additionally, in the F 1s spectra (Figs. 5b and 5e), both separators show a LiF signal at ~684.5 eV^[46]. Compared to the CG group, the PAP separator

sample exhibits a stronger peak corresponding to Li_xPO_yF_z/PF₆⁻ complexes, suggesting enhanced LiPF₆ degradation into anion-derived species that strengthen the CEI and improve its endurance under elevated temperatures.

Cryo-TEM images (Figs. 5g and 5i) further reveal the structural differences between CEIs formed using the two separators. The PAP group shows a thin, uniform CEI that closely conforms to the LCO surface, with a well-defined boundary, indicating a self-limiting, compositionally regulated interphase, consistent with the *in situ* EIS results (Fig. S8 in Supplementary Material). In contrast, the CG group develops a substantially thicker CEI, reflecting uncontrolled buildup of decomposition products.

The uniform distribution of inorganic fragments (e.g., $\text{Li}_2F_3^-$ and LiPO_3^{2-}) indicates the formation of a hybrid CEI, where a robust LiF-rich framework ensures thermal and mechanical stability, while $\text{Li}_x\text{PO}_yF_z$ species provide chemical resistance against hydrofluoric acid corrosion, collectively sustaining

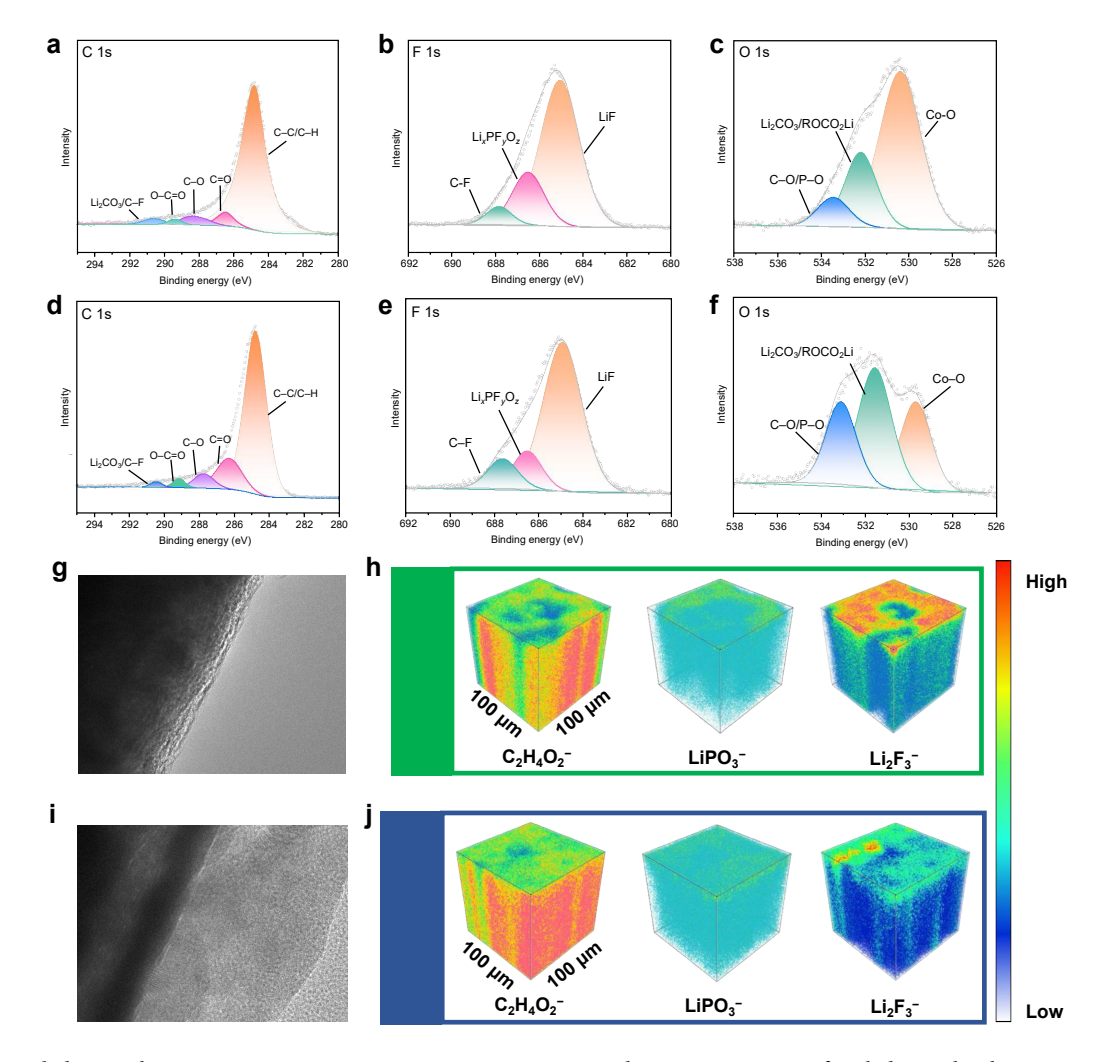


Figure 5 Cycled LCO characterization on separator impact. C 1s, F 1s and O 1s XPS spectra of cycled LCO by the PAP separator (a–c) and the CG separator (d–f). Cryo-TEM images of cycled LCO by the PAP separator (g) and the CG separator (i). TOF-SIMS three-dimensional distributions of cycled LCO by the PAP separator (h) and the CG separator (j) for $C_2H_4O_2^-$, $LiPO_3^{2-}$ and $Li_2F_3^-$ fragments.

interfacial integrity under elevated-temperature conditions^[37,47]. As shown in Fig. 5h, the PAP exhibits localized yet moderate organic signals, reflecting controlled solvent decomposition, alongside uniform and dense inorganic fragment distributions consistent with efficient LiPF₆ decomposition into stable inorganic components. Conversely, the CG exhibits heterogeneous and intense organic distributions indicative of rampant solvent degradation—together with sparse, clustered inorganic signals, suggesting incomplete inorganic phase formation (Fig. 5j). These results highlight that the PAP separator leverages its PEI/PI-induced interfacial solvation structure. By optimizing ion-solvent interactions, it promotes the formation of a thin, inorganic-rich CEI that guides controlled electrolyte decomposition toward inorganic species (e.g., Li₂F₃- and LiPO₃²⁻), while simultaneously suppressing excessive organic byproduct accumulation. This results in a precisely regulated CEI with superior thermal stability, which is critical for sustaining high-voltage battery operation at elevated temperatures.

4 Conclusion

In this work, we designed a gradient-functionalized PAP separator with a PEI/PI outer coating, demonstrating an effective strategy to regulate interfacial solvation structures and enhance the performance of high-voltage LIBs at elevated temperatures. The PEI/PI coating, featuring strong polar interactions via C=O and C-N groups, interacts with Li⁺ to weaken its solvation sheath, lower the desolvation energy, and accelerate Li+ transport across the interface. The PEI/PI layer not only enhances the separator's wettability, thermal stability, and mechanical strength but also directs controlled electrolyte decomposition, producing a homogeneous, inorganicrich, and thermally stable CEI on the LCO surface. Consequently, the LCO||Li battery with the PAP separator delivers markedly enhanced long-term cycling performance, with an average Coulombic efficiency of 99.4% after 200 cycles under 4.6 V and 60°C. The key findings highlight that regulating the interfacial solvation structure via separator coating represents a crucial pathway to achieving highperformance high-voltage LIBs, offering design principles for future development. While this study confirms the effectiveness of the PEI/PI coating in stabilizing high-voltage LCO cells, potential longterm issues such as PEI degradation, mechanical fatigue, or delamination under extended cycling remain challenges that require further investigation. For instance, improving the coating's resistance to interfacial byproducts, such as by incorporating functional additives or dopants, offers a promising strategy to extend its effectiveness in regulating the interfacial chemistry and thereby further advance the longevity of high-voltage batteries.

Acknowledgements

None.

Author contribution statement

Shuofeng Jian: Planning, conducting experimental work, discussion, writing and editing. Jiahui Zeng: Planning, conducting experimental work, discussion, writing and editing. Chen Guo: Discussion, experimental work and editing. Zhaohuang Zhan: Discussion, experimental work and editing. Yumeng Lan: Discussion, experimental work and editing. Zu-Wei Yin: Discussion, experimental work and editing. Hai Lin: Discussion, supervision, paper revision. Luyi Yang: Discussion, supervision, paper revision, funding acquisition. Feng Pan: Discussion, supervision, funding acquisition, paper revision. All the authors have approved the final manuscript.

Data availability

Data will be made available from the corresponding author on request.

Declaration of competing interest

Chen Guo is the employee of Shenzhen Senior Technology Material Co., LTD. All the other contributing authors report no conflicts of interest in this work.

Funding

This work was supported by the Shenzhen Science and Technology Planning Project (Grant No. JSGG20220831095604008), the National Natural Science Foundation of China (Grant No. 51902296), the National Center for International Research of Electric Vehicle Power Batteries and Materials (Grant No. 2015B01015), the Guangdong Key Laboratory of Design and Calculation of New Energy Materials (Grant No. 2017B030301013), and the Shenzhen Key Laboratory of New Energy Resources Genome Preparation and Testing (Grant No. ZDSYS201707281026184).

Use of AI statement

None.

Electronic Supplementary Material: Supplementary material is available in the online version of this article at https://doi.org/10.26599/EMD.2025.9370077

References

[1] Xing, F. F., Liao, S. H., Qin, J. Q., Wang, G. R., Zheng, S. H., Wu, Z. S. (2024). Regulating the nanosize effect of

- LiCoO₂ for high-performance battery-supercapacitor hybrid devices. *ACS Energy Lett.* 9, 355–362.
- [2] Janek, J., Zeier, W. G. (2016). A solid future for battery development. *Nat. Energy* 1, 16141.
- [3] Lee, M. J., Han, J., Lee, K., Lee, Y. J., Kim, B. G., Jung, K. N., Kim, B. J., Lee, S. W. (2022). Elastomeric electrolytes for high-energy solid-state lithium batteries. *Nature* 601, 217–222.
- [4] Jaumaux, P., Wu, J. R., Shanmukaraj, D., Wang, Y. Z., Zhou, D., Sun, B., Kang, F. Y., Li, B. H., Armand, M., Wang, G. X. (2021). Non-flammable liquid and quasi-solid electrolytes toward highly-safe alkali metal-based batteries. *Adv. Funct. Mater.* 31, 2008644.
- [5] Wu, S. L., Yu, Z. F., Nie, X. L., Wang, Z. H., Huang, F. L., Wei, Q. F. (2022). Fast ion conduction nanofiber matrix composite electrolyte for dendrite-free solid-state sodiumion batteries with wide temperature operation. *Adv. Energy Mater.* 12, 2202930.
- [6] Ye, L. H., Li, X. (2021). A dynamic stability design strategy for lithium metal solid state batteries. *Nature* 593, 218–222.
- [7] Yuan, B. T., Feng, Y. H., Qiu, X. H., He, Y. H., Dong, L. W., Zhong, S. J., Liu, J. P., Liang, Y. F., Liu, Y. P., Xie, H. D., et al. (2024). A safe separator with heat-dispersing channels for high-rate lithium-ion batteries. *Adv. Funct. Mater.* 34, 2308929.
- [8] Xu, Z. X., Zhang, X. Y., Yang, J., Cui, X. Z. X., Nuli, Y., Wang, J. L. (2024). High-voltage and intrinsically safe electrolytes for Li metal batteries. *Nat. Commun.* 15, 9856.
- [9] Luo, H. Y., Ji, X. Y., Zhang, B. D., Chen, M., Wu, X. H., Zhu, Y. L., Yu, X. Y., Wang, J. H., Zhang, H. T., Hong, Y. H., et al. (2024). Revealing the dynamic evolution of electrolyte configuration on the cathode-electrolyte interface by visualizing (De) solvation processes. *Angew. Chem. Int. Ed.* 63, e202412214.
- [10] Shi, C. Y., Li, Z. G., Wang, M. R., Hong, S., Hong, B., Fu, Y. X., Liu, D., Tan, R., Wang, P. S., Lai, Y. Q. (2025). Electrolyte tailoring and interfacial engineering for safe and high-temperature lithium-ion batteries. *Energy Environ. Sci.* 18, 3248–3258.
- [11] Zhang, S., Guan, D. C., Xue, Z. Y., Shen, C. Y., Shen, Y. Y., Hu, G. R., Cao, Y. B., Peng, Z. D., Wang, W. G., Ren, Y., et al. (2025). Enhanced elevated-temperature performance of LiMn₂O₄ cathodes in lithium-ion batteries via a multifunctional electrolyte additive. *Chem. Eng. J.* 503, 158219.
- [12] Li, Z. J., Zhao, W. G., Ren, H. Y., Yi, H. C., Du, Y. H., Yu, H. T., Fang, J. J., Song, Y. L., Chen, H., Zhou, L., et al. (2024). Tuning surface reconfiguration for durable cathode/electrolyte interphase of LiCoO₂ at 45°C. Adv. Energy Mater. 14, 2402223.
- [13] Zhou, T. T., Tang, W. H., Lv, J. W., Deng, Y. R., Liu, Q., Zhang, L., Liu, R. P. (2023). Yolk–shell structured ST@Al₂O₃ enables functional PE separator with enhanced Lewis acid sites for high-performance lithium metal batteries. *Small* 19, 2303924.
- [14] Wang, K., Zhao, T., Lv, R. X., Tang, W. M., Yu, T. Y., Li,

- L., Wu, F., Chen, R. J. Lithium metal batteries enabled by ion flux-regulating coating on separator. *Adv. Funct. Mater.* in press.
- [15] Fan, Z. X., Chen, X. Y., Shi, J. J., Nie, H., Zhang, X. M., Zhou, X. P., Xie, X. L., Xue, Z. G. (2025). Functionalized separators boosting electrochemical performances for lithium batteries. *Nano-Micro Lett.* 17, 128.
- [16] Dong, G. Q., Dong, N. X., Liu, B. X., Tian, G. F., Qi, S. L., Wu, D. Z. (2020). Ultrathin inorganic-nanoshell encapsulation: TiO₂ coated polyimide nanofiber membrane enabled by layer-by-layer deposition for advanced and safe highpower LIB separator. J. Membr. Sci. 601, 117884.
- [17] Chen, S. M., Zhao, W. G., Zheng, G. R., Yang, C. Y., Chen, T. W., Ren, H. Y., Zuo, Y., Yao, X. M., Li, K., Xue, H. Y., et al. Engineering durable interphases for high-voltage Liion batteries under thermal stress. *Natl. Sci. Rev.* in press.
- [18] Rahman, M. M., Mateti, S., Cai, Q. R., Sultana, I., Fan, Y., Wang, X. W., Hou, C. P., Chen, Y. (2019). High temperature and high rate lithium-ion batteries with boron nitride nanotubes coated polypropylene separators. *Energy Stor*age Mater. 19, 352–359.
- [19] Shi, C., Dai, J. H., Shen, X., Peng, L. Q., Li, C., Wang, X., Zhang, P., Zhao, J. B. (2016). A high-temperature stable ceramic-coated separator prepared with polyimide binder/Al₂O₃ particles for lithium-ion batteries. *J. Membr. Sci.* 517, 91–99.
- [20] Lin, G., Jia, K., Bai, Z. X., Liu, C. C., Liu, S. N., Huang, Y. M., Liu, X. B. (2022). Metal-organic framework sandwiching porous super-engineering polymeric membranes as anionphilic separators for dendrite-free lithium metal batteries. *Adv. Funct. Mater.* 32, 2207969.
- [21] Xu, R. M., Kang, Y., Zhang, W. M., Zhang, X. W., Pan, B. C. (2022). Oriented UiO-67 metal-organic framework membrane with fast and selective lithium-ion transport. *Angew. Chem. Int. Ed.* 61, e202115443.
- [22] Song, Y. Z., Liu, X., Ren, D. S., Liang, H. M., Wang, L., Hu, Q., Cui, H., Xu, H., Wang, J. L., Zhao, C., et al. (2022). Simultaneously blocking chemical crosstalk and internal short circuit via gel-stretching derived nanoporous nonshrinkage separator for safe lithium-ion batteries. Adv. Mater. 34, 2106335.
- [23] Wang, Y., Guo, M. H., Fu, H., Wu, Z. Z., Zhang, Y. Z., Chao, G. J., Chen, S. L., Zhang, L. S., Liu, T. X. (2022). Thermotolerant separator of cross-linked polyimide fibers with narrowed pore size for lithium-ion batteries. *J. Membr. Sci.* 662, 121004.
- [24] Lu, Z. H., Sui, F., Miao, Y. F., Liu, G. H., Li, C., Dong, W., Cui, J., Liu, T. X., Wu, J. X., Yang, C. L. (2021). Polyimide separators for rechargeable batteries. *J. Energy Chem.* 58, 170–197.
- [25] Hussain, A., Islam, M. M., Shah, S. S., Zahir, M. H., Ahammad, A. J. S., Aziz, M. A. (2025). Recent progress in polyetherimide membrane for high-performance lithium batteries. *J. Energy Storage* 131, 117584.
- [26] Chen, S. M., Zheng, G. R., Yao, X. M., Xiao, J. L., Zhao, W. G., Li, K., Fang, J. J., Jiang, Z. N., Huang, Y. X., Ji, Y. C., et al. (2024). Constructing matching cathode–anode

- interphases with improved chemo-mechanical stability for high-energy batteries. *ACS Nano* 18, 6600–6611.
- [27] Lu, H. T., Du, A., Lin, X. P., Zhang, Z. Y., Liu, S. S., Xie, Y. S., Li, W. H., Song, J. W., Lu, Y. H., Chen, W., et al. (2024). Rationally coupling thermal tolerance, thermal conductance, and overheating-response in a separator for safe batteries. *Energy Environ. Sci.* 17, 7860–7869.
- [28] Kresse, G., Furthmüller, J. (1996). Efficient iterative schemes for *ab initio* total-energy calculations using a planewave basis set. *Phys. Rev. B* 54, 11169–11186.
- [29] Kresse, G., Furthmüller, J. (1996). Efficiency of ab-initio total energy calculations for metals and semiconductors using a plane-wave basis set. *Comput. Mater. Sci.* 6, 15–50.
- [30] Grimme, S. (2004). Accurate description of van der Waals complexes by density functional theory including empirical corrections. *J. Comput. Chem.* 25, 1463–1473.
- [31] Perdew, J. P., Burke, K., Ernzerhof, M. (1996). Generalized gradient approximation made simple. *Phys. Rev. Lett.* 77, 3865–3868.
- [32] Blöchl, P. E. (1994). Projector augmented-wave method. *Phys. Rev. B* 50, 17953–17979.
- [33] Wang, V., Xu, N., Liu, J. C., Tang, G., Geng, W. T. (2021).
 VASPKIT: A user-friendly interface facilitating high-throughput computing and analysis using VASP code.
 Comput. Phys. Commun. 267, 108033.
- [34] Grimme, S., Ehrlich, S., Goerigk, L. (2011). Effect of the damping function in dispersion corrected density functional theory. *J. Comput. Chem.* 32, 1456–1465.
- [35] Momma, K., Izumi, F. (2011). VESTA 3 for three-dimensional visualization of crystal, volumetric and morphology data. J. Appl. Crystallogr. 44, 1272–1276.
- [36] Lin, G., Bai, Z. X., Liu, C. C., Liu, S. N., Han, M. G., Huang, Y. M., Liu, X. B. (2022). Mechanically robust, nonflammable and surface cross-linking composite membranes with high wettability for dendrite-proof and high-safety lithium-ion batteries. *J. Membr. Sci.* 647, 120262.
- [37] Spampinato, V., Auditore, A., Tuccitto, N., Vitale, R., Bellocchi, G., Galliano, F., Rascunà, S., Arena, G., Licciardello, A. (2024). Physico-chemical characterization of polyimide passivation layers for high power electronics applications. *Appl. Surf. Sci.* 670, 160719.
- [38] Zhang, C. X., Lu, Z., Song, M., Zhang, Y. Q., Jing, C. Y., Chen, L. B., Ji, X. B., Wei, W. F. (2023). Highly oxidationresistant ether gel electrolytes for 4.7 V high-safety lithium

- metal batteries. Adv. Energy Mater. 13, 2203870.
- [39] Chen, Y. Q., He, Q., Mo, Y., Zhou, W., Zhao, Y., Piao, N., Liu, C., Xiao, P. T., Liu, H., Li, B. H., et al. (2022). Engineering an insoluble cathode electrolyte interphase enabling high performance NCM811//graphite pouch cell at 60°C. Adv. Energy Mater. 12, 2201631.
- [40] Huang, H., Li, Z. Q., Gu, S., Bian, J. C., Li, Y. Z., Chen, J. J., Liao, K. M., Gan, Q. M., Wang, Y. F., Wu, S. S., et al. (2021). Dextran sulfate lithium as versatile binder to stabilize high-voltage LiCoO₂ to 4.6 V. *Adv. Energy Mater.* 11, 2101864.
- [41] Liu, X. M., Zhao, L. L., Xu, H. R., Huang, Q. S., Wang, Y. Q., Hou, C. X., Hou, Y. Y., Wang, J., Dang, F., Zhang, J. T. (2020). Tunable cationic vacancies of cobalt oxides for efficient electrocatalysis in Li–O₂ batteries. *Adv. Energy Mater.* 10, 2001415.
- [42] Ji, Y. C., Huang, Y. X., Dong, Z. H., Fang, J. J., Liu, P., Liu, S. Q., Cao, A. M., Xue, H. Y., Chen, S. M., Qiu, J. M., et al. (2025). Anion adsorption at the inner-helmholtz plane directs cathode electrolyte interphase formation. *Angew. Chem. Int. Ed.* 64, e202425535.
- [43] Wang, L. L., Ma, J., Wang, C., Yu, X. R., Liu, R., Jiang, F., Sun, X. W., Du, A. B., Zhou, X. H., Cui, G. L. (2019). A novel bifunctional self-stabilized strategy enabling 4.6 V LiCoO₂ with excellent long-term cyclability and high-rate capability. *Adv. Sci.* 6, 1900355.
- [44] Yang, K. C., Liu, Z. L., Chai, J. C., Zheng, Y., Fu, X. N., Shen, Y. H., Chen, J., Liu, Z. H., Shi, S. W. (2022). High performance polyimide-based separator for 4.5V high voltage LiCoO₂ battery with superior safety. *Mater. Chem. Phys.* 282, 125975.
- [45] Huang, H. T., Chen, K. J., Li, C. Y., Zhou, Z. X., Wang, W. H., Deng, B., Liu, S. W., Qian, C., Yue, M., Chi, Z. G., et al. (2024). Zwitterion grafted polyimide separator for improving lithium-ion transport and its application in LiCoO₂ batteries. *Chem. Eng. J.* 481, 148577.
- [46] Di, L., Yufang, C., Weiwei, S., Wei, X., Shuaiyu, Y., Shiqiang, L., Lanlan, Z., Yanshuang, Z., Tianyan, Y., Peitao, X., et al. (2023). Cathode electrolyte interface engineering by gradient fluorination for high-performance lithium rich cathode. *Adv. Energy Mater.* 13, 2301765.
- [47] Zhou, C. H., Liu, Y., Mei, P., Zhang, Y., Ai, B., Hong, L. X., Cheng, T., Zhang, W. Electrostatic catalysis-driven asymmetric SEI for dendrite-free lithium metal anodes. *Adv. Funct. Mater.* in press.